catalysts

MDPI

Article

Crystalline ZnO Photocatalysts Prepared at Ambient Temperature: Influence of Morphology on *p*-Nitrophenol Degradation in Water

Julien G. Mahy [1,*,†], Louise Lejeune [1,†], Tommy Haynes [1], Nathalie Body [1], Simon De Kreijger [1], Benjamin Elias [1], Raphael Henrique Marques Marcilli [2], Charles-André Fustin [2] and Sophie Hermans [1,*]

[1] Molecular Chemistry, Materials and Catalysis (MOST), Institute of Condensed Matter and Nanosciences (IMCN), Université Catholique de Louvain, Bâtiment Lavoisier. Pl. Louis Pasteur 1, 1348 Louvain La Neuve, Belgium; l.lejeune@student.uclouvain.be (L.L.); tommy.haynes@uclouvain.be (T.H.); nathalie.body@uclouvain.be (N.B.); simon.dekreijger@uclouvain.be (S.D.K.); benjamin.elias@uclouvain.be (B.E.)

[2] Bio and Soft Matter Division (BSMA), Institute of Condensed Matter and Nanosciences (IMCN), Université Catholique de Louvain, Place Louis Pasteur 1, 1348 Louvain-la-Neuve, Belgium; raphael.marques@uclouvain.be (R.H.M.M.); charles-andre.fustin@uclouvain.be (C.-A.F.)

* Correspondence: julien.mahy@uclouvain.be (J.G.M.); sophie.hermans@uclouvain.be (S.H.); Tel.: +32-4-3664771 (J.G.M.); +32-10-47-28-10 (S.H.)

† These two authors participated equally to the research.

Citation: Mahy, J.G.; Lejeune, L.; Haynes, T.; Body, N.; De Kreijger, S.; Elias, B.; Marcilli, R.H.M.; Fustin, C.-A.; Hermans, S. Crystalline ZnO Photocatalysts Prepared at Ambient Temperature: Influence of Morphology on *p*-Nitrophenol Degradation in Water. *Catalysts* 2021, *11*, 1182. https://doi.org/10.3390/catal11101182

Academic Editor: Magdalena Janus

Received: 20 August 2021
Accepted: 27 September 2021
Published: 28 September 2021

Abstract: Since the Industrial Revolution, technological advances have generated enormous emissions of various pollutants affecting all ecosystems. The detection and degradation of pollutants has therefore become a critical issue. More than 59 different remediation technologies have already been developed, such as biological remediation, and physicochemical and electrochemical methods. Among these techniques, advanced oxidation processes (AOPs) have been popularized in the treatment of wastewater. The use of ZnO as a photocatalyst for water remediation has been developing fast in recent years. In this work, the goals are to produce ZnO photocatalysts with different morphologies, by using a green sol-gel process, and to study both the influence of the synthesis parameters on the resulting morphology, and the influence of these different morphologies on the photocatalytic activity, for the degradation of an organic pollutant in water. Multiple morphologies were produced (nanotubes, nanorods, nanospheres), with the same crystalline phase (wurtzite). The most important parameter controlling the shape and size was found to be pH. The photoactivity study on a model of pollutant degradation shows that the resulting activity is mainly governed by the specific surface area of the material. A comparison with a commercial TiO_2 photocatalyst (Evonik P25) showed that the best ZnO produced with this green process can reach similar photoactivity without a calcination step.

Keywords: aqueous sol-gel process; ZnO; photocatalysis; pollutant degradation

1. Introduction

Although too often poorly appreciated and considered as an almost inexhaustible resource, water is becoming a scarce commodity [1]. Its excessive and disproportionate use in some regions of the world, combined with the overall increase in the population, adds increasing pressure on water reserves and increases the general level of aqueous pollution. To face these problems, treating and decontaminating wastewater for reuse appears to be a promising solution [2–4].

In general, it is possible to distinguish the following three main families of water contaminants: chemical contaminants (organic and inorganic), microbial contaminants, such as viruses and bacteria, and, finally, radiological contaminants. Depending on the

type and quantity of pollutants present, as well as the volume of water to be treated, various treatment methods can be used [5]. This work will focus on organic pollutants and the associated degradation processes.

Recently, innovative water pollution control techniques have emerged, as a result of water quality legislation strengthening. Among these, advanced oxidation processes (AOPs) are attracting growing interest. These processes constitute promising alternatives for the degradation of organic pollutants, which are non-biodegradable and refractory to conventional treatments [6].

All AOP technologies are based on the production and use of hydroxyl radicals (OH•), which represent the most powerful oxidizing species that can be used in the field of water and industrial effluent treatment. The advantage of AOPs lies in their ability to degrade almost all organic molecules, by reacting with –C=C– double bonds and by attacking aromatic nuclei, which are major constituents of refractory pollutants. Due to their ability to break down the most recalcitrant compounds into biologically degradable molecules and/or mineral compounds (CO_2 and H_2O), they can be used in addition to conventional techniques, such as adsorption on activated carbon, reverse osmosis, or biological treatments [6].

Among AOPs, photocatalysis relies on the activation of a semiconductor-type photocatalyst with light energy. When the photons meet the surface of the photocatalyst, they are absorbed by the material, which allows the production of highly reactive oxidizing and reducing species on the surface of the semiconductor photocatalyst. These radicals, generated near the catalyst surface, from water and dissolved oxygen, are then able to attack chemical bonds and induce the total or partial destruction of a wide variety of organic compounds [6–8].

Among the different semiconductors that can be used in photocatalysis, ZnO has drawn a lot of attention in the photocatalytic remediation of wastewater fields, due to its high free-exciton binding energy (60 meV), high electrical conductivity, and strong redox ability with valence (VB) and conduction (CB) band positions [7,9]. Moreover, ZnO presents chemical and thermal stability [10].

ZnO is a semiconductor with a band gap of around 3.37 eV [7], so it is activated by UV light. As for the archetypal TiO_2, many studies have been conducted to modify ZnO light absorption properties, in order to shift it in the visible range or to increase its photoactivity in the UV range [11–13]. Different preparation methods are found to synthesize ZnO photocatalysts, such as the sol-gel method, precipitation, microwave-assisted methods, or thermal oxidation [9,10,14–16]. Sol-gel methods present the advantages of occurring under soft conditions (i.e., at a low temperature and low pressure), producing liquid sol or solid gel, to obtain materials in different shapes, such as coatings, powders, or monoliths, and this process is also often compatible with water as solvent, reducing the environmental impact of the preparative steps [8,17–19]. The sol-gel process is based on the hydrolysis and condensation of metal alkoxides, to produce metal oxide materials [18]. By playing on different parameters, such as the pH, the catalyst, or the time of reaction, fine tuning of the metal oxide material characteristics (nanostructure, morphology, or surface properties) can occur [17,20,21].

To date, the photocatalytic applications of ZnO nanostructures have been investigated by numerous researchers. However, relatively little is known about the performance of ZnO catalysts in relation to their morphologies, in a systematic comparative manner [7].

In this work, the goals will be to produce ZnO photocatalysts with different morphologies, by using a green sol-gel process, and to study both the influence of the synthesis parameters on the resulting morphology, and the influence of these different morphologies on the photocatalytic activity for the degradation of an organic pollutant in water. To reach these goals, an aqueous sol-gel synthesis of ZnO will be studied, and the impact of three synthesis parameters (pH, stirring, time of reaction) will be analyzed using a design

of experiment (DoE) plan, implemented with JMP® Pro 15 software. All the ZnO photocatalysts will be characterized by PXRD (powder X-ray diffraction), TEM (transmission electron microscopy), XPS (X-ray photoelectron spectroscopy), nitrogen adsorption–desorption measurements, and DRUVS (diffuse reflectance UV–visible spectroscopy). In the last part of this study, the photocatalytic activities of ZnO materials will be assessed on the degradation of a water model pollutant that is commonly found in the pesticide *p*-nitrophenol (PNP). The resulting photoactivities will be compared with the well-known commercial Evonik Aeroxide P25 TiO_2 photocatalyst. This commercial product is synthesized by a high-temperature aerosol process [22].

2. Results and Discussion

As explained in Section 3.1, different protocols were followed, in order to obtain ZnO nanoparticles (NPs) with different morphologies. Two different synthesis protocols were used, named syntheses 1 and 2 in the following, to facilitate reading. Synthesis 1 is a sol-gel method carried out at room temperature, using NaOH as basic titrant, and is adapted from [9], while synthesis 2 is a sol-gel method performed at 60 °C, using KOH as the basic titrant and absolute EtOH as a solvent, and is adapted from [10].

2.1. Synthesis 1: a Study of Three Reaction Parameters

First, ZnO NPs were prepared by the synthesis 1 protocol, as detailed in Section 3.1.1. The following three main reaction parameters were studied: the pH, which was varied from 8 to 12.5, the stirring (or not) of the solution, and the reaction duration (varied between 1 and 7 days). In order to accurately reveal the joint impact of these three factors on the size response, an experimental plan was designed using JMP® Pro 15 software. The tested conditions are detailed in Table 1.

Table 1. Experimental plan designed by JMP® 15 software.

Table	Code name	pH	Time (days)	Stirring
1	Z1	10.25	7	No
2	Z2	10.25	1	Yes
3	Z3	12.5	4	No
4	Z4	8	4	Yes
5	Z5	12.5	1	No
6	Z6	8	7	Yes
7	Z7	12.5	1	Yes
8	Z8	8	7	No
9	Z9	12.5	7	Yes
10	Z10	8	1	No
11	Z11	12.5	1	No
12	Z12	8	7	Yes
13	Z13	12.5	7	Yes
14	Z14	8	1	No
15	Z15	12.5	7	No
16	Z16	8	1	Yes
17	Z17	10.25	4	Yes
18	Z18	10.25	4	No

2.1.1. Phase Composition

The crystalline ZnO phase present in all samples was identified by means of PXRD, as can be observed in Figure 1, which shows the diffraction pattern of one of the 18 ZnO samples (Z13). The position of the recorded diffraction peaks corresponds to that of the ZnO bulk diffraction spectrum, which can be indexed as hexagonal wurtzite (JCPDS 36-

1451). The (004) and (202) plane peaks are less visible than the reference peaks because of the background noise. All the other 17 samples exhibit the same XRD patterns, with various peak widths, indicative of different crystallite sizes. Some XRD patterns (Figure S1 as an example) show additional peaks in the 2θ range of 5°–25°. After an extra washing with deionized water, these peaks disappear, which suggests that they are relative to a zinc acetate residue and not to another ZnO phase. Thanks to the Scherrer formula (Equation (1)), it is possible to calculate the crystallite size (d_{XRD}) of the 18 ZnO samples from their diffraction patterns (Table 2, d_{XRD} (nm)). The full width at half maximum (FWHM, named β) is calculated for the (102) plane (fourth peak), and θ is the angle corresponding to this diffraction plane. β and θ were taken directly from the EVA software that was provided with the PXRD instrument.

$$d_{XRD} = 0.9 \frac{\lambda}{\beta \cos(\theta)} \quad (1)$$

where β is the full width of the peak at half maximum, after correction of the instrumental broadening (rad), λ the wavelength (nm), and θ the Bragg angle (rad).

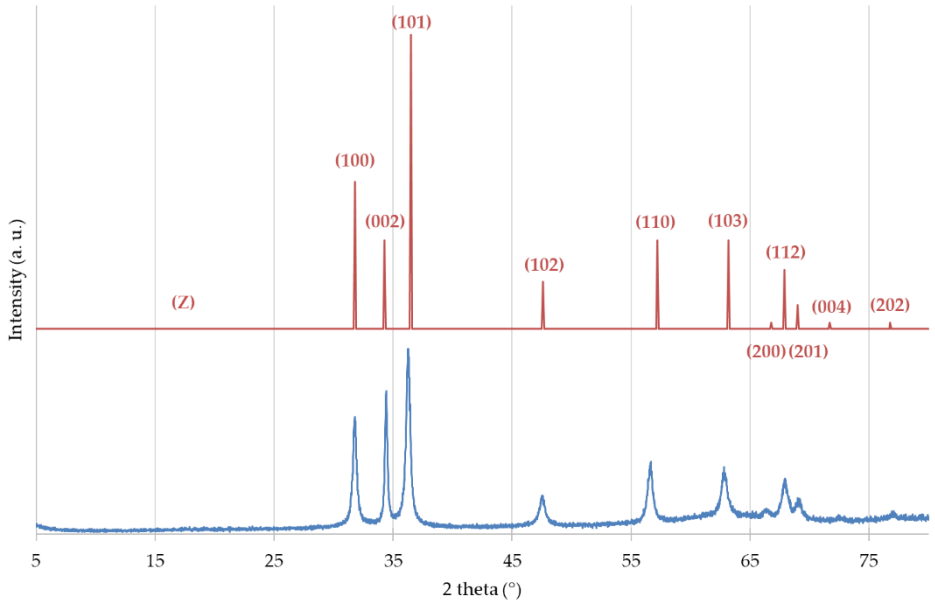

Figure 1. XRD diffraction pattern obtained for a ZnO sample prepared by Synthesis 1 (Z13-blue line), as compared to a wurtzite reference (JCPDS 36-1451) diffraction spectrum (Z-red line).

All the samples were also analyzed by XPS, which confirmed the ZnO composition. All the samples presented the same XPS spectra (an example is given in Supplementary Materials, Figure S2).

2.1.2. Morphology and Size

The ZnO NPs morphology of the 18 samples was investigated by TEM analysis. As is shown for nine samples in Figure 2, ZnO NPs can present the following variety of morphologies: spherical, elongated, or geometrical (rectangular, trapezoidal). Most of them were agglomerated in bigger particles. The morphology of the agglomerates is even more significantly different; they either have perfect geometry, such as spheres or regular hexagons, or smaller and more irregular shapes.

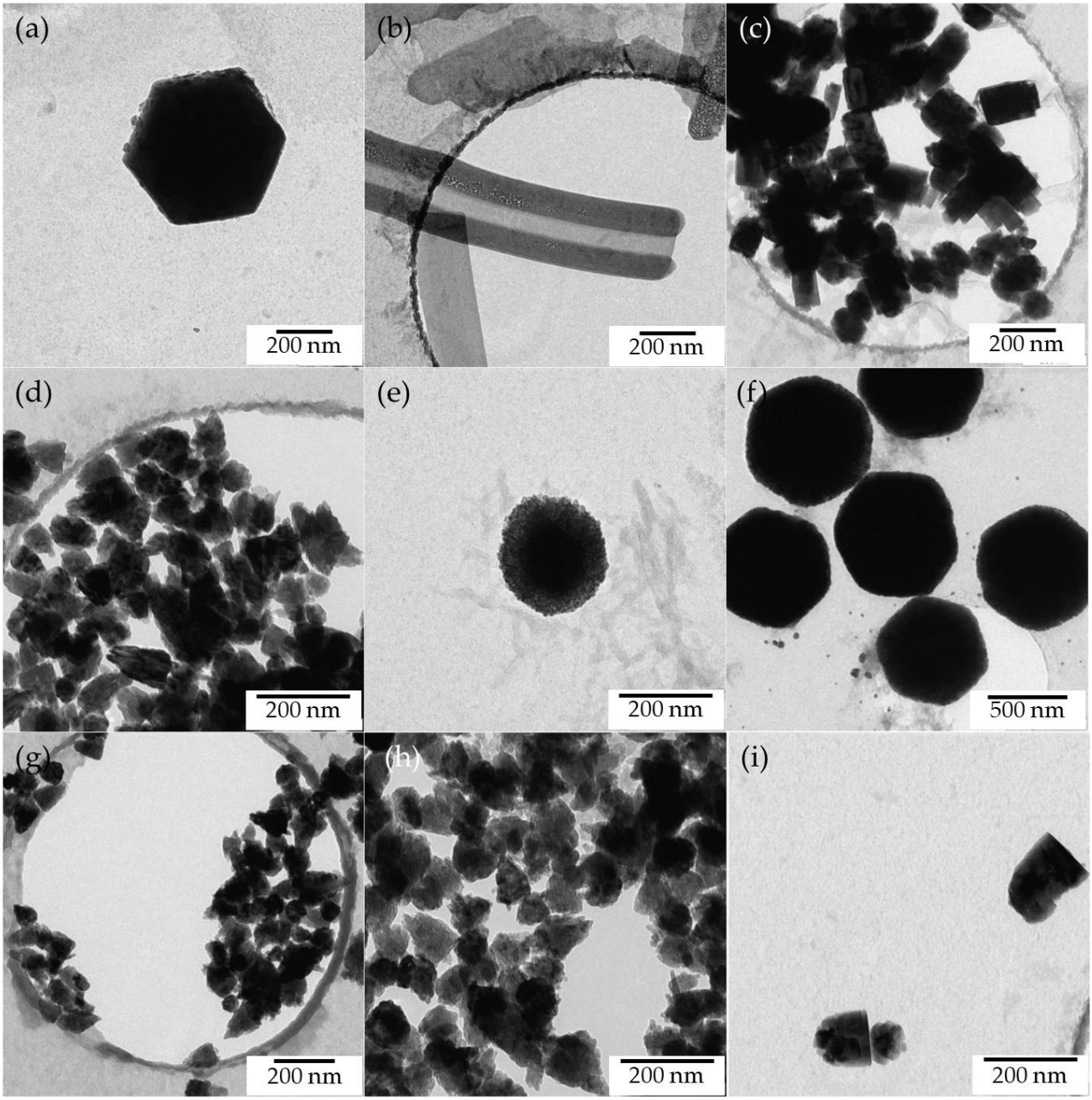

Figure 2. TEM images of nine ZnO samples (**a**) Z4 (**b**) Z10 (**c**) Z1 (**d**) Z15 (**e**) Z17 (**f**) Z14 (**g**) Z2, (**h**) Z13 and (**i**) Z18 in which different morphologies of the obtained NPs and agglomerates can be clearly appreciated. The different code names correspond to the different syntheses (see Table 2).

Table 2. Concerning NPs and agglomerates exhibiting a non-spherical morphology, the measured d_{TEM} corresponds to the height for triangular or trapezoidal shapes, the length for the rectangular or elongated shapes and the diameter of the circumscribed circle for the regular hexagonal shapes.

Table 2. Overview of the crystallite size (d_{XRD}) calculated from diffraction patterns and average size of NPs and of their agglomerates (d_{TEM}), and the related standard deviations (σ_{TEM}) measured from TEM images for the 18 syntheses included in the design of experimental plan. The diameter d_{TEM} for non-spherical NPs and agglomerates corresponds to the height, the length and the diameter of the circumscribed circle of triangular or trapezoidal, rectangular and regular hexagonal morphologies, respectively.

JMP N°	Code Name	d_{XRD} (nm)	d_{TEM} Nanoparticle (nm)	σ_{TEM} (nm)	d_{TEM} Agglomerate (nm)	σ_{TEM} (nm)	Morphology Nanoparticle	Morphology Agglomerate
1	Z1	32	41	13	138	34	rectangular	geometrical
2	Z2	52	29	8	109	36	elongated	triangular and spherical
3	Z3	23	30	8	109	41	elongated	triangular and spherical
4	Z4	109	28	15	717	115	spherical	hexagonal
5	Z5	21	25	10	91	25	elongated	triangular and spherical
6	Z6	124	125	53	414	166	geometrical	spherical and geometrical
7	Z7	18	20	5	100	29	spherical	triangular and spherical
8	Z8	71	48	12	1015	458	spherical	geometrical
9	Z9	19	28	10	104	30	elongated	triangular and spherical
10	Z10	105	-	-	110	26	tubular	tubular
11	Z11	23	25	7	96	31	spherical	triangular and spherical
12	Z12	110	126	-	451	130	spherical	geometrical
13	Z13	19	20	7	91	25	elongated	triangular and spherical
14	Z14	104	30	15	771	97	spherical	hexagonal
15	Z15	19	21	8	98	32	elongated	triangular and spherical
16	Z16	112	37	5	696	134	spherical	hexagonal
17	Z17	46	9	5	203	53	spherical	spherical
18	Z18	48	37	19	158	57	rectangular	geometrical

- = not measured.

Differences between the diameters calculated from diffraction patterns and those measured from TEM images are observable. It is difficult to indiscriminately compare the sizes measured from XRD and TEM analyses. First of all, the sizes measured by XRD and TEM do not have the same meaning. Indeed, by means of the Scherrer formula (Equation (1)), an average crystallite size is determined, while from TEM images, the size of NPs or agglomerates of a specific zone of the sample can be measured. This is a fact that is important to keep in mind when the d_{XRD} is smaller than the d_{TEM}, which means that several crystallites constitute a single NP. If the comparison of d_{XRD} and d_{TEM} gives the same numbers, it shows that the observed nanoparticles are mainly composed of only one crystallite.

Secondly, an important approximation of the Scherrer equation is that all the crystallites are considered as being spherical. As observed in Figure 2, it is clear that not all the morphologies are spherical.

Moreover, a bias between the observed size, as compared to the real size, occurs for both the size determination techniques employed [23]. Since a TEM image is a 2D projection of the sample, the latter could be slightly distorted, depending on its orientation, and thus the size on the projection is not exactly the same as the actual object. Concerning XRD, for the Scherrer calculations to be meaningful, the diffraction peak width should be

purely that of the material itself, and should consequently be free from side effects. The following several factors, other than NP sizes, could contribute to the width of the peaks: instrumental broadening or the use of a non-monochromatic X-ray source, inhomogeneous strain or crystal lattice imperfections, temperature factors, etc. [24,25]. Furthermore, crystallite size broadening is more important at a large value of 2θ, while instrumental width and microstrain broadening are also the largest at a high 2θ value. The asymmetry of the peaks is more pronounced at a 2θ angle lower than 30° [24,25]. As a compromise, the (102) diffraction plane located at a 2θ value of 48° was chosen to be used in the Scherrer calculations. Thus, the d_{XRD} determined is the apparent size of the crystallites in the direction perpendicular to the (102) plane.

Finally, as previously mentioned, the NPs prepared with synthesis 1 are agglomerated in bigger particles of various sizes and shapes. Therefore, the precise measurement of a single NP is intricated in TEM images. It is noteworthy that the standard deviations of the mean sizes of both NPs and agglomerates measured by TEM are really high, whereas XRD provided a single average value of crystallite size, without any estimation of the size distribution. A more complex variant of the Scherrer equation can be developed, to take into account the crystallite size distribution [25], but it was not considered in this work. The Scherrer equation is thus useful to compare several samples with each other, rather than to precisely quantify the absolute size.

On the basis of the values gathered in Table 2, the d_{XRD} and d_{TEM} values are compared and found to correspond, to a certain extent. Nevertheless, concerning the reactions performed at pH 8 (samples Z4, Z10, Z8, Z6, Z12, Z14, and Z16), TEM and XRD analyses exhibit the biggest differences. Reactions at a low pH seem to be less reproducible than reactions at a higher pH. It was not possible to measure an isolated NP on the TEM images of the Z10 sample. Indeed, as observed in Figure 2b, only long tubular forms were visible.

2.1.3. Statistical analysis of the three tested parameters

In order to study the influence of the three tested parameters (pH, stirring, and reaction time) in this synthesis 1 protocol (Table 1), a statistical analysis was performed using the JMP® Pro 15 software. It was chosen to work with crystallite sizes that were determined from XRD patterns, rather than size measured on TEM images. Indeed, the approximations of the Scherrer equation, as described in Equation (1), would have impacted all the size values in the same way, while it was difficult to precisely measure the NP size on TEM images, due to their agglomeration in bigger particles, and to anisotropy. To visualize the relationships between the three tested parameters and the d_{XRD} response, a scatter plot was drawn (Figure 3) for the 18 ZnO experiments. A marked correlation between pH and d_{XRD} is appreciated in Figure 3 (middle), while stirring and reaction time do not seem to influence the d_{XRD} obtained.

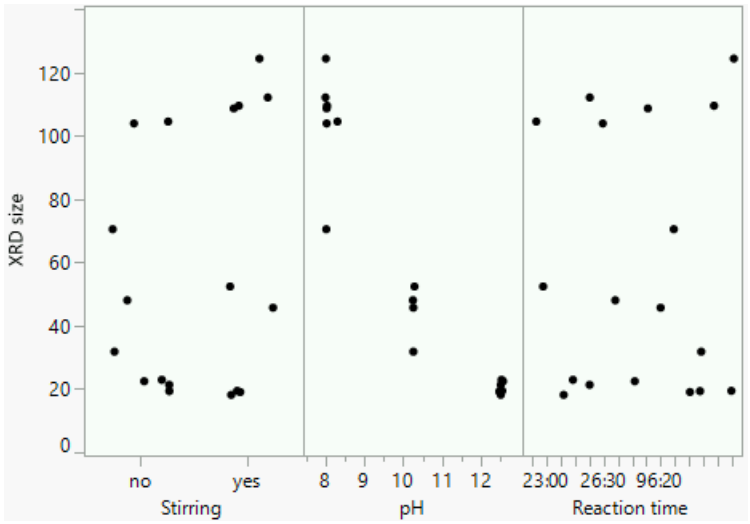

Figure 3. Scatter plot of d_{XRD} values in function of stirring, pH and reaction time. A correlation between d_{XRD} and pH is clearly observable.

To investigate the percentage of correlation between the pH and d_{XRD}, further statistical analyses were performed. The actual pH of the 18 launched experiments varied by a few tenths of a unit from the expected pH of the designed JMP® plan, because of the accuracy of the pH meter. For the statistical analyses, all the pH values were standardized to the theoretical values of 8.0, 10.25, and 12.5, in order to reduce the repeatability error. Then, a statistical model was built as follows: using a model of a degree equal to two, a standard least squares method, and a screening report.

Figure 4 is a plot of the obtained d_{XRD}, using the Scherrer formula to identify the d_{XRD} values expected by the built model. The adjustment summary is gathered in Table 3. The R^2 is equal to 0.97, meaning that 97% is explained by the built model, which is therefore relevant. The analysis of variance report (Table 4) provides the calculations for comparing the fitted model to a model where all the predicted values are equal to the response mean (58.5578 nm). The degree of freedom is the number of parameters implemented to fit the model. This degree is equal to six for the model, for the following parameters: pH, stirring, reaction time, pH * pH, pH * stirring, and pH * reaction time. The parameters (stirring * reaction time) and (reaction time * reaction time) were not implemented here. An analysis including these two additional parameters was also performed (see Figure S3 and S4, and Table S1 in Supplementary Materials). Nevertheless, the LogWorth of the pH was lower and the error sum of squares was higher, which means that the model explained less than the analysis performed with less parameters.

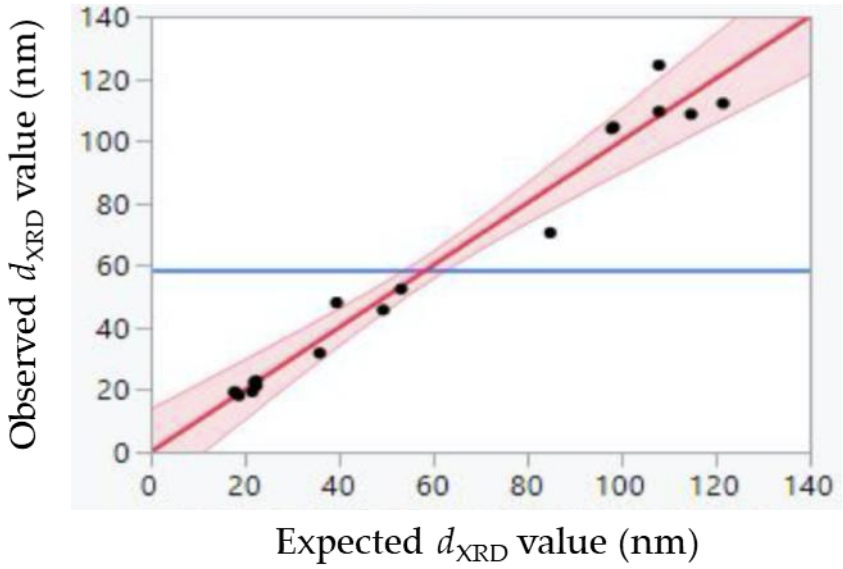

Figure 4. Observed d_{XRD} values in function of expected d_{XRD} by the built model. The red area and the blue line represent the confidence interval and the mean value of the d_{XRD}, respectively.

Table 3. Adjustment summary.

Term	Value
R^2	0.9715
Adjusted R^2	0.9559
Square root of the mean error	84.968
Mean of the response	585.578
Number of observations	18

Table 4. Analysis of variance report.

Source	Degree of freedom	Sum of squares	Mean square	F ratio	Prob >F
Model	6	27,042.891	4,507.15	624.301	<0.0001
Error	11	794.146	72.20	-	-
Corrected total	17	27,837.037	-	-	-

The total sum of squares is the sum of the squared differences between the response values and the sample mean. It represents the total variation in response values (27,837.037). The error sum of squares is the sum of squared differences between the fitted values and the actual values. It represents the variability that remains unexplained by the model (794.146). The model sum of squares is the difference between the total sum of squares and the error sum of squares; therefore, it represents the variability explained by the model [26]. In this case, the variability explained by the model is equal to 27,042.891, which is much higher than 794.146, which remained unexplained. The mean square is the sum of squares divided by the related degree of freedom.

The F ratio is a statistical test, the ratio between the model and the error mean squares. The Probaility. >F is the P-value of the F test. The P-value is used to quantify the statistical significance of a result under a null hypothesis. P-value is a measure of the probability of obtaining an F ratio as large as what is observed. In other words, a very small P-value means that such an extreme observed outcome would be very unlikely under the null hypothesis [26]. Here, the Prob.> F is lower than 0.0001, which indicates that there is at least one significant effect in the model.

Figure 5 shows the importance of each parameter in the model (P-value and LogWorth). The LogWorth is defined as-$\log_{10}$(P-value), this is a transformation adjusting P-values to provide an appropriate scale for graphing. Generally, a P-value lower than 0.01 corresponds to a presumption against the null hypothesis that is very high [26]. The reference blue line represents the -$\log_{10}(0.01)$, which is equal to two. A parameter that has a LogWorth value greater than two is therefore considered significant. Assuming these considerations, the most influencing effect on the crystallite size is the pH; a LogWorth equal to 8.812 and an exact P-value of 1.5×10^{-9} were obtained. To a lesser extent, the second parameter (pH*pH) also possesses a LogWorth value higher than two. On the basis of this analysis, we can conclude that the ZnO crystallite size depends on the pH, and that the function has a slight quadratic component (pH^2). Because of the significance of the model, it is possible to predict the d_{XRD} for chosen values of the three parameters, using the prediction profiler.

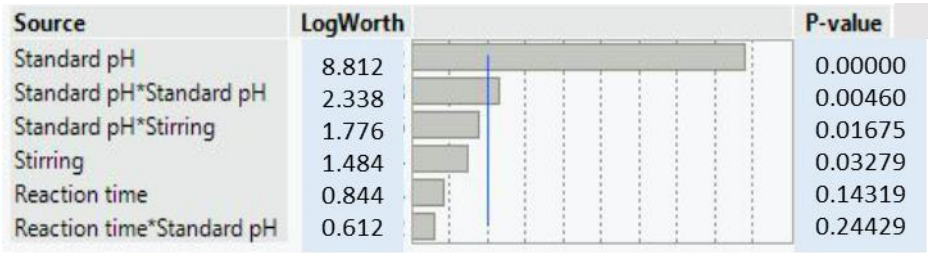

Figure 5. Effects summary. The blue line represents the LogWorth reference equal to two.

These results are consistent with the observations made during the experiments. Indeed, the clear solution transformed into a milky white suspension after the addition of the first drops of NaOH. Nucleation begins immediately, because of the insolubility of ZnO crystallites in the solution. Thus, stirring and reaction time do not have much impact. Whereas, the higher the pH, the higher the NaOH concentration, and, therefore, the higher the supersaturation of the solution, which leads to faster nucleation. When the pH is

lower, the concentration of NaOH in the solution is lower as well, and the crystallites can grow slower and are therefore bigger.

2.2. Synthesis 2

ZnO NPs were also prepared by a second protocol, as described in Section 3.1.2., giving sample Z19. The obtained NPs were also characterized by PXRD and TEM analyses. The aim of using this second synthesis is to produce regular spherical NPs with a maximum size of 10 nm.

The collected diffraction peaks (Figure 6) are in very good agreement with the wurtzite reference (JCPDS = 36-1451). The d_{XRD} calculated by the Scherrer equation, using the (102) peak plane as well, is equal to 8 nm (Table 5).

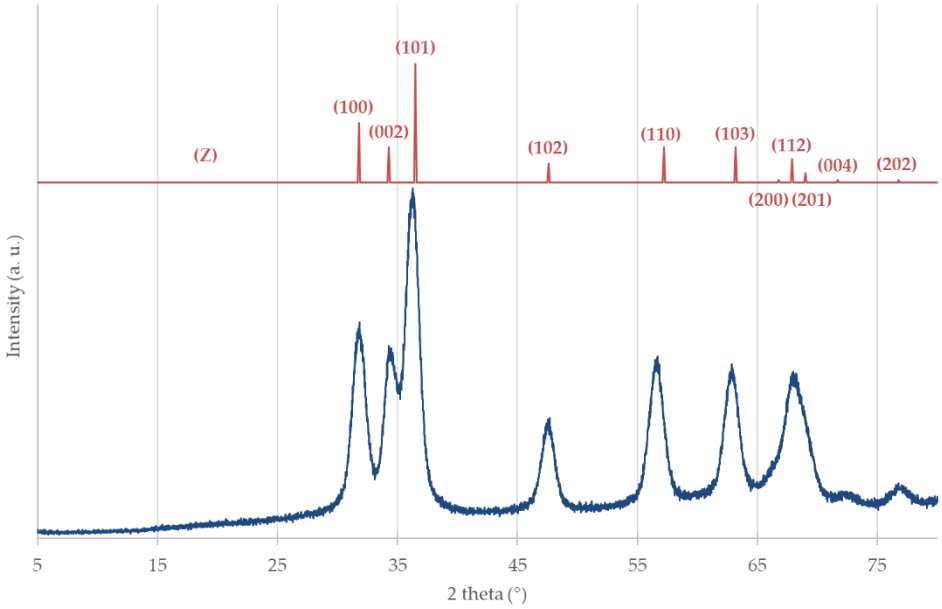

Figure 6. XRD diffraction pattern obtained for ZnO sample (Z19) prepared by synthesis 2 (blue line) as compared to a wurtzite reference diffraction spectrum (Z-red line).

The Z19 sample was also analyzed by XPS, which confirmed the ZnO composition (Figure S2).

TEM analyses were performed both for the sample before any washing, and after the washing steps and redispersion in technical EtOH. The TEM images (Figure 7a) revealed that most of the NPs are spherical and well dispersed. Since the NPs are dispersed, the size measurement of individual NPs (d_{TEM}) was performed using ImageJ® software, in order to increase the precision. The obtained average size of NPs is 5 nm (σ = 1 nm), close to the d_{XRD} calculated by the Scherrer formula. On the TEM image after the washing steps (Figure 7b), NPs were found to be agglomerated into clusters of an average size of 113 nm (σ = 70). This result suggests that the centrifugation between each washing step may induce aggregation of the NPs.

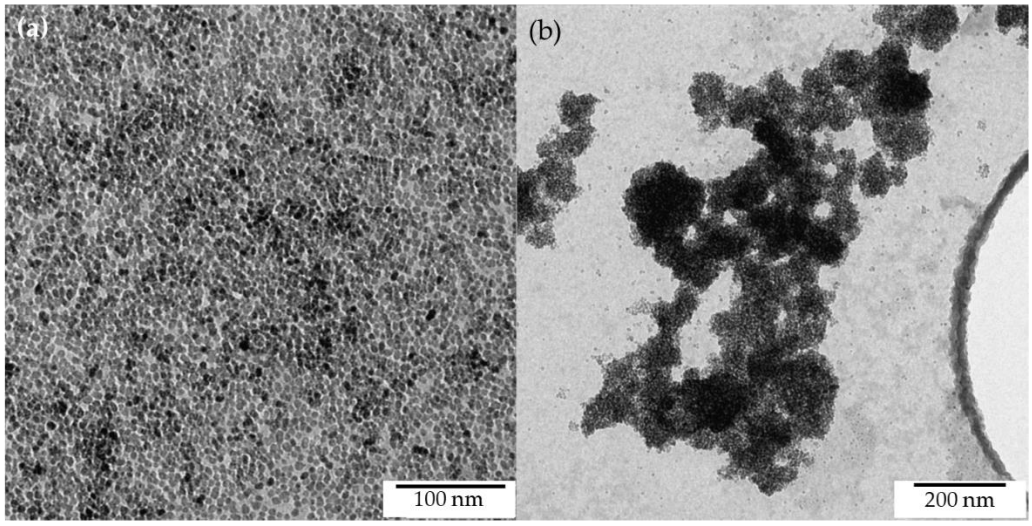

Figure 7. TEM images of ZnO sample (Z19) prepared by synthesis 2. (**a**) Sample analyzed before washing steps, NPs are well dispersed; (**b**) sample analyzed after washing steps, NPs are agglomerated in particle clusters.

In the article reporting the protocol that we adapted for this second synthesis, Shamhari et al. [10] emphasize that the utilization of absolute EtOH as a solvent is required to produce NPs with a uniform shape and size. Therefore, a variant of this synthesis, using technical EtOH as a solvent, was also performed, in order to study the influence of the EtOH grade during the reaction process.

As shown in Figure 8, NPs prepared using technical EtOH (Z20), and after washing steps, have the same morphology as those in the case of the synthesis performed in absolute EtOH. The average NPs size is 5 nm (σ = 2 nm), which is comparable to the first synthesis test using absolute EtOH (Z19). Therefore, the grade of the EtOH used as a solvent does not impact the morphology and size of the prepared NPs. As compared to NPs synthesized in absolute EtOH, analyzed before any washing and redispersion steps, the NPs are less well dispersed compared to when absolute EtOH is used as a solvent. This result seems to confirm the hypothesis that ZnO NP aggregation occurs during the centrifugation and washing steps.

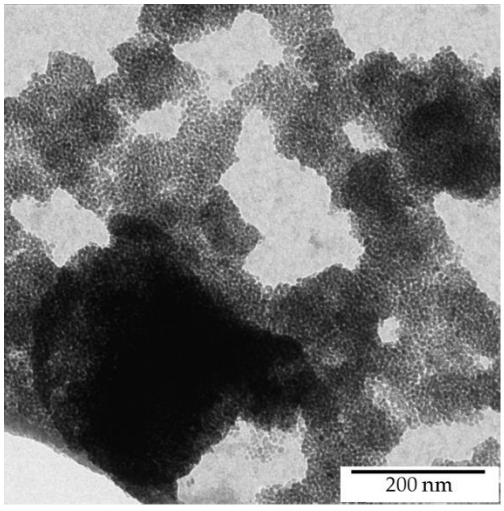

Figure 8. TEM image of ZnO sample (Z20) prepared by a variant of synthesis 2 using technical EtOH as a solvent, after washing steps.

2.3. Comparison of both Synthesis Methods

In order to compare the two ZnO syntheses performed, Table 5 gathers the mean reaction parameters (pH, basic titrant, temperature (T)), the crystallite size formed (d_{XRD}), and their morphology, as observed on TEM images. As discussed in Section 2.1.3., pH is the most influencing parameter on the d_{XRD}, in the case of synthesis 1. As a comparison, the pH in synthesis 2 is also shown in Table 5. At the same pH value, different particle sizes were obtained using both methods. The reaction medium of synthesis 2 became iridescent after 2 h, while the reaction mediums of the others turned into a milky white solution right after the addition of the very first drops of the basic titrant. ZnO crystallization seems to be slower during synthesis 2, and, therefore, KOH is a basic titrant that is more appropriate for the synthesis of smaller ZnO NPs. The higher temperature also allows better solubility of zinc salt, and reduces the agglomeration.

Table 5. Comparison of the main reaction parameters of the two ZnO syntheses, the crystallite size (d_{XRD}) and the morphology observed by TEM.

Synthesis	pH	Basic titrant	Temperature (°)	d_{XRD} (nm)	NPs Shape
1	8.00	NaOH	25	105	geometrical
1	10.25	NaOH	25	45	geometrical
1	12.50	NaOH	25	20	spherical
2	10.16	KOH	60	8	spherical

2.4. Photocatalytic Activity

Among different semiconductors, ZnO is a successful and popular photocatalyst that has demonstrated high photosensitivity and chemical stability [27,28]. As developed in Sections 2.1 and 2.2, a large variety of ZnO nanostructures were obtained from the different syntheses. Because the influence of the morphology of ZnO nanostructures on their photocatalytic activity is not fully investigated in the literature, it seemed interesting to test some of the prepared ZnO samples in such applications. In this case, the tests were performed under UV-A light because of the high band gap value of ZnO (>3 eV).

The degradation percentage of *p*-nitrophenol (PNP, structure presented in Figure 9), D_{PNP}, is given in Equation (2) [29], where $[PNP]_t$ is the concentration in PNP at time t and $[PNP]_0$ is the initial concentration of PNP at time t = 0.

$$D_{\mathrm{PNP}}\ (\%) = \left(1 - \frac{[PNP]_t}{[PNP]_0}\right) \times 100\% \quad (2)$$

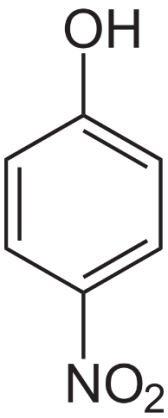

Figure 9. Structure of PNP molecule.

2.4.1. Experiments under two UV-A lamps

In order to study the influence of the morphology of the ZnO NPs on the photocatalytic activity, different ZnO samples, prepared with synthesis 1 and 2, exhibiting different nanoshapes, were selected to be tested (Figure 2 and 7). The experimental methods are detailed in Section 3.3. Samples Z2 and Z13 exhibit the same morphology (triangular aggregates), but their sizes are not the same (Z2:29 nm; Z13:20 nm) (Table 2). This is why they were both chosen. The others are either nanotubes (Z10), faceted (Z18), round aggregates (Z17), hexagonal aggregates (Z14), or very small spherical NPs (Z19).

First, a blank test was performed as follows: PNP was irradiated alone under UV-A light, in order to determine whether its degradation occurs after 7 h of light exposure. Figure S5 shows the PNP absorption spectra for PNP, as follows: not irradiated; irradiated with UV-A light during 7 h non-filtered; the same, but filtered with the same syringe filter as used for the catalysts; and filtered, followed by the addition of a drop of HNO_3 (1 $mol.L^{-1}$), respectively. As observed in Figure S5, PNP is not degraded upon 7 h of UV-A light exposure. The filter (polypropylene, 13 mm diameter, 0.2 m pore size, Whatman™) does not adsorb the PNP. Thus, this filter can be used in further tests.

The photocatalytic activity of the seven selected ZnO samples for PNP degradation was tested under two UV-A lamps. The degradation percentage of PNP (D_{PNP}) was calculated using Equation (2), and the results are gathered in Figure 10. Commercial Evonik P25 TiO_2 was also tested as a reference. Indeed, it is the most used commercial photocatalyst, and no commercial ZnO photocatalyst is available to date.

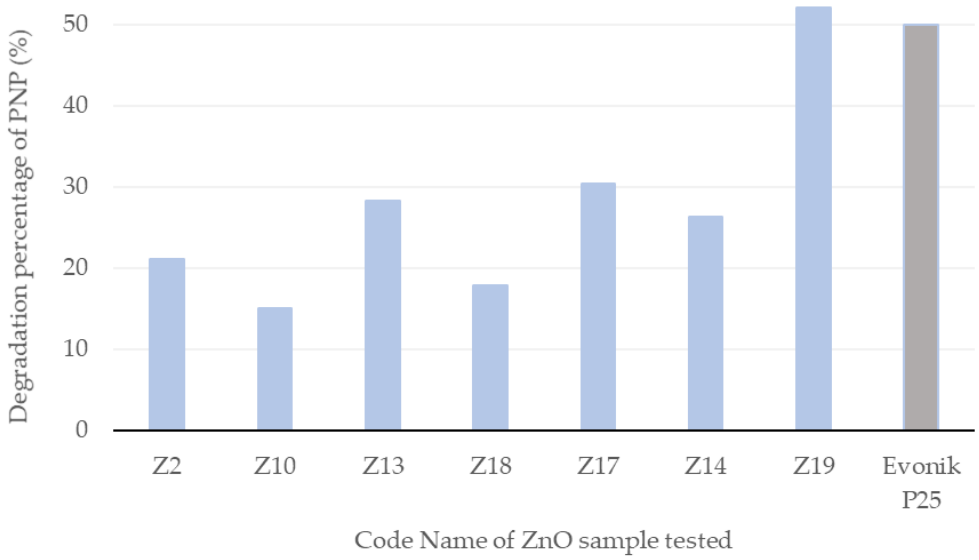

Figure 10. Degradation percentage of PNP (%) for the 7 ZnO samples tested (under two UV-A lamps) and for commercial Evonik P25 TiO_2 used as reference.

The best results were obtained with Z19 (D_{PNP} = 52%), which presented the smallest particle sizes. The second highest PNP degradation percentage (D_{PNP} = 30%) was connected to the Z17 sample, whose particle size (9 nm) was similar to that of Z19, but these were agglomerated into bigger particles (203 nm), as can be appreciated from Figure 2e. The descending D_{PNP} order for the other ZnO samples tested approximately followed the order of the NPs size, as follows: Z13 (20 nm) > Z14 (30 nm) > Z2 (29 nm) > Z18 (37 nm). The sample that provided the lowest PNP degradation rate was Z10. Indeed, as shown in Figure 2b, the morphology of the ZnO structure in this case is long and tubular. The best photocatalyst (Z19) has similar activity to commercial Evonik P25 (~50% after 7 h). It is

important to be reminded that this commercial photocatalyst is made by a high-temperature aerosol process [22], while the ZnO samples presented here are made at low temperature, without a calcination step.

2.4.2. Specific Surface Area and Optical Properties

In order to obtain the values of the direct band gap energy ($E_{g;direct}$) and the specific surface area of the NPs, which are two important parameters of semiconductor photocatalysts, diffuse reflectance ultraviolet–visible spectroscopy (DRUVS) and 5 points Brunauer–Emmett–Teller (BET) surface area analyses were performed on the seven ZnO samples selected for the photocatalytic tests, and also on commercial Evonik P25.

From DRUVS, it is possible to determine the $E_{g;direct}$ by plotting $(F(R_\infty)h\upsilon)^2$ as a function of the photon energy, and by extrapolating the linear part of the curve to the intersection with the x-axis (Equations (5) and (6) from [29]). For commercial TiO_2, it is the indirect band gap that is calculated, as TiO_2 is an indirect semiconductor [30].

Figure 11 shows the plot of $(F(R_\infty)h\upsilon)^2$ as a function of the photon energy $h\upsilon$ for the seven ZnO samples tested. Table 6 gathers the results of the band gap energies found. All the ZnO samples possess a slightly different $E_{g;direct}$ value, which is similar to values found in the literature (~3.2 eV) [9,31]. There is no correlation between $E_{g;direct}$ and NP size in this case. The light used for the photocatalytic tests is UV-A light, and its spectrum extends from a wavelength of 400 nm to 315 nm, which corresponds to 3.10 eV to 3.93 eV. Therefore, the $E_{g;direct}$ of each sample is compatible with UV-A light activation, which is why all the samples were active photocatalysts, and were able to degrade PNP.

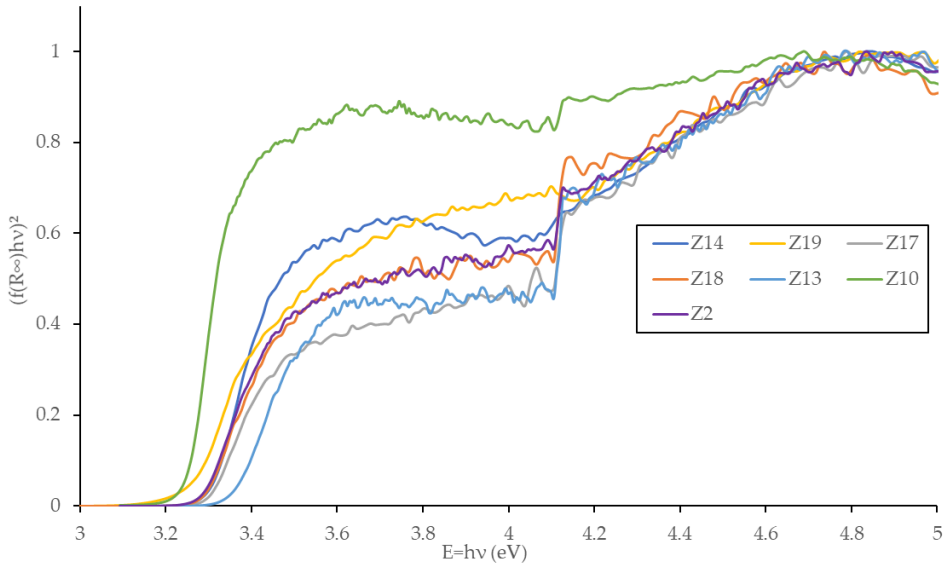

Figure 11. Determination dy DRUVS of the direct band gap energy for the seven ZnO samples tested in photocatalysis.

Table 6. Band gap energy ($E_{g,direct}$), PNP degradation efficiency (D_{PNP}), surface area from 5 points BET (S_{BET}) and corresponding calculated value (S_{th}) for the seven ZnO samples. S_{th} was not calculated for Z10 due to its tubular morphology not allowing the NPs size to be measured from TEM images.

Code name	S_{BET} ($m^2\ g^{-1}$)	S_{th} ($m^2\ g^{-1}$)	D_{PNP} (%)	D_{PNP}/S_{BET}	$E_{g,direct}$ (eV)
Z2	5	20	21	4.2	3.28
Z10	4	*	15	3.8	3.25
Z13	23	56	28	1.2	3.36

Z18	4	22	18	4.5	3.28
Z17	6	23	30	5.0	3.30
Z14	3	10	26	8.7	3.29
Z19	30	129	52	1.7	3.26
Evonik P25	55	77	50	0.9	3.05**

* = not determined, indeed for Z10 samples the tubular morphology is not compatible with the model.

** For commercial Evonik P25 TiO_2, it is the indirect band gap that is calculated.

From the 5 points nitrogen physisorption measurements, it is possible to determine the value of BET surface area ($m^2.g^{-1}$). Table 6 gathers the results provided by the nitrogen adsorption 5 points BET (S_{BET}), as compared to the theoretical model surface (S_{th}) calculated by Equation (3), for the seven ZnO samples tested in photocatalysis, and for Evonik P25.

$$S_{\text{th}} = \frac{3}{\rho * r} \quad (3)$$

where S_{th} ($m^2.g^{-1}$) is the theoretical model surface area; ϱ ($g.m^{-3}$) is the density, a value of 5.61 $g.cm^{-3}$ was taken for ZnO [32], and a value of 3.89 $g.cm^{-3}$ for TiO_2 [22]; and r is the radius (m) of the crystallite. Here, it is chosen to take r as the radius determined by PXRD (i.e., $d_{XRD}/2$).

As shown in Table 6, the highest surface area measured by BET is for the sample Z19, which was expected, according to its high PNP degradation result. The S_{BET} and S_{th} values are consistent with each other, even if all the S_{BET} values measured are much lower than expected. This is probably due to the agglomeration of NPs in larger aggregates in the dried powders, which results in a decrease in the specific surface area. Indeed, the specific surface area is inversely proportional to the size of NPs, and agglomerated particles decrease the apparent size of NPs. The calculation of the S_{th} also has some of the following limitations: all the NPs are considered spherical, which is not always the case (Z18 for example), and all the NPs are considered monodispersed. Nevertheless, it can give an idea of the importance of agglomeration in the samples, and its impact on the specific surface area measurements. It can be concluded that the photocatalytic activity is mainly governed by the available surface of NPs. Commercial Evonik P25 presented the highest specific surface area (~55 $m^2.g^{-1}$).

If the activity is normalized by the specific surface area (Table 6, fifth column), the order of photoefficiency is different, and all the ZnO samples are better than the commercial P25 catalyst. Especially, the Z14 sample, composed of hexagon, presents a high normalized photoefficiency that is ten times higher than P25. These results suggest that if the surface area of the ZnO samples could be increased, an activity much higher than the one of Evonik would be obtained.

Some ways to increase the specific surface area would be, for example, to use some surfactant during the synthesis, which would create additional porosity inside the ZnO materials, due to a templating effect. A thermal treatment of the synthesized samples could also create some microporosity if unreacted reagents were still present. However, the temperature of such a treatment must be optimized in order to avoid sintering of the particles, which would increase the particle sizes and decrease the specific surface area. Another way to increase the specific surface area would be to synthesize smaller nanoparticles below 5 nm, but these would be more difficult to recover.

2.4.3. Experiments under four UV-A Lamps with the Best ZnO Photocatalyst

The ZnO NPs prepared by synthesis 2 (Z19), which possess an average NPs size of 8.3 nm, were the best photocatalysts among all the ZnO samples tested, due to their higher specific surface area. The photocatalytic activity of Z19 was, therefore, also tested under

four UV-A lamps, in order to enhance the PNP degradation. After 7 h under four UV-A lamps, Z19 exhibited a DPNP equal to 80%, which is a very competitive result.

2.4.4. Recycling Experiments with the Best ZnO photocatalyst

To assess the stability of the ZnO material, recycling experiments were conducted with the Z19 sample, knowing that ZnO suffers from photocorrosion [13]. In Table 7, the results of three consecutive photoactivity tests on PNP degradation are presented, with the mean value and the standard deviation of these numbers. The degradation activity remained constant during the three experiments, showing that the material kept its integrity for 21 h. Moreover, an XRD measurement was taken on the Z19 sample, after the three experiments. The pattern (Figure S6) was the same as in Figure 6, showing that the material maintained its crystallinity during the recycling experiments.

Table 7. Recycling photocatalytic experiments on PNP degradation with Z19 sample.

Sample	1st photocatalytic experiment (Figure 10) (%)	2nd photocatalytic experiment (%)	3rd photocatalytic experiment (%)	Mean PNP degradation value (%)	Standard deviation
Z19	52	47	49	48	3

Concerning the evolution of the samples while working with real samples of polluted water, carbon contamination of the surface of ZnO materials can occur during degradation, depending on the concentration of pollutants to eliminate. This contamination can be removed by regeneration of the catalyst with UV exposition, or a thermal treatment if the amount is very high.

3. Materials and Methods

All the chemical reagents and solvents (purity and their supplier) used are gathered in alphabetic order hereafter: Ammonium hydroxide(25% in water, extrapure, Acros Organics, Fisher Scientific, Hampton, NH, USA), Ethanol (99%, EURO DENATURATED Techni Solv®, VWR Chemicals, Radnor, PA, USA), Ethanol absolut (AnalaR NORMAPUR® Reag. Ph. Eur.,VWR Chemicals, Radnor, PA, USA), Methanol (Technical, VWR Chemicals, Radnor, PA, USA), Nitric acid (68%, VWR Chemicals, Radnor, PA, USA), *p*-Nitrophenol (99%, Acros Organics, Fisher Scientific, Hampton, NH, USA), Potassium hydroxide (>85% for laboratory use, Ph. Eur., Chem-Lab NV, Zedelgem, Belgium), Sodium Hydroxide (99%, AnalaR NORMAPUR® Reag. Ph. Eur., VWR Chemicals, Radnor, PA, USA), Zinc acetate dihydrate (99,5%, for analysis, E. Merck, Fort kennerworth, NJ, USA).

3.1. ZnO Synthesis

Zinc oxide NPs were synthesized by means of different methods in order to obtain different morphologies. The parameters influencing the ZnO crystallite sizes have been studied.

3.1.1. Sol-gel Synthesis 1

Zinc oxide (ZnO) NPs were first synthesized based on a sol-gel method reported by Alias et al. [9]. In a 250 mL Erlenmeyer flask, 20 mmol of zinc acetate dihydrate ($Zn(CH_3COO)_2.2H_2O$) was dissolved into 100 mL of EtOH at room temperature by magnetic stirring. In order to study the influence of the pH, the agitation and the reaction time on the ZnO crystallite size, an experimental design (Table 1) was performed assisted by JMP Pro 2015 software (JMP 12, SAS, Cary, NC, USA, 2015). The pH of the solution was followed (Electrode pH, BlueLine, SI ANALYTICS®, Servilab) during the titration by sodium hydroxide solution ($NaOH$ 1mol.L^{-1}). The clear solution transformed into a milky

white suspension immediately after the addition of the first drops of NaOH. After the predefined reaction time, under or without stirring, the product was extracted by centrifugation (ALC® centrifuge PK 120, 6000 RPM, 10 min, ALC international S.r.l., Cologno Monzese, Italy) and washed twice with deionized water and twice with EtOH. The product was dried at 120°C overnight and ground with a mortar and pestle.

3.1.2. Sol-gel Synthesis 2

ZnO NPs were also prepared following the solvo-thermal procedure reported by Shamhari et al. [10]. In a 250 mL Erlenmeyer flask, 6.7 mmol of $Zn(CH_3COO)_2.2H_2O$ was dissolved in 63 mL of absolute EtOH and heated to 60 °C using a liquid oil bath with constant magnetic stirring. In a second flask, 13.2 mmol of potassium hydroxide (KOH) was dissolved in 33 mL of absolute ethanol under the same conditions as zinc acetate dihydrate. When both dissolutions were complete, KOH solution was added drop by drop into the zinc acetate dihydrate solution at 60 °C with vigorous stirring. The reaction mixture was stirred for 3 h at 60 °C. The solution turned iridescent and then a white precipitate formed. The product was separated by centrifugation (ALC® centrifuge PK 120, 9000 RPM, 30 min) and washed twice with deionized water and twice with ethanol. The obtained product was dried at 120 °C overnight and ground with a mortar and pestle.

3.2. Material Characterizations

X-ray diffraction patterns were recorded with a D8 Advance (Bruker, USA) diffractometer, a Cu-Kα (0.15409 Å) anode and a LynxEye detector. A few milligrams of each sample were deposited on an epoxy sample holder, previously covered with a very thin layer of commercial moisturizer (Nivea®). Data were collected in the 2θ range from 5° to 80°, with a step of 0.15° and a time/step of 0.15 s at room temperature. The obtained 2D diffractograms were analyzed using DIFFRAC.EVA software (Bruker, Billerica, USA); they were azimuthally integrated using the Fit2D software and calibrated with a LaB6 standard diffractogram.

The Scherrer formula (Equation (1)) was used to estimate the nanoparticle crystallite size, d_{XRD} (nm) [8].

Nitrogen sorption measurements were performed on a Micromeritics ASAP 2020 instrument (Bruker) in order to determine the BET specific surface area (S_{BET}). About a hundred milligrams of solid sample were degassed at 120 °C for 6 h prior to analysis.

Transmission electron microscopy was performed on an LEO 922 OMEGA energy filter transmission electron microscope operating at 120 kV. Sample preparation consisted of dispersing a few milligrams of each sample into an appropriate solvent, using sonication (VWR ultrasound cleaner, power level 9, 30 min). Then, a few drops of the supernatant were placed on a holed carbon film deposited on a copper grid (CF-1.2/1.3-2 Cu-50, C-flat™, Protochips, Morrisville, NC, USA). The grid was then carefully deposited on a filter paper and dried overnight under vacuum at room temperature. About one hundred particles were measured and an average value was estimated (d_{TEM}).

DRUVS analyses were performed on a UV 3600 Plus UV–VIS–NIR spectrophotometer from Shimadzu Kyoto Japan. Measurements were performed in diffuse reflectance mode. The spectra range of analysis was from 200 to 600 nm. The baseline was realized using Spectralon as a reference. The solid sample preparation consisted of filling the 3 mm diameter microsampling cup using the appropriate funnel (praying mantis™ sampling kit, Harrick). The sample was then flattened with a microscope glass slide and then introduced into the praying mantis™. The spectra were transformed using the Kubelka–Munk function [22,33] to produce a signal, normalized for comparison between samples, enabling the band gaps ($E_{g,direct}$) to be calculated. The details of this treatment method were widely described elsewhere [23,29].

XPS analyses were performed with a FISONS SSI-X-probe 100/206 spectrometer (Surface Science Instruments), equipped with an electron beam (8 keV) for surface charge neutralization. A few milligrams of each sample were deposited on a double-sided adhesive

support, clung onto a brass cup, and then introduced into a Macor® carousel topped by a nickel grid in order to avoid charge effects. The analyses were then performed, without further sample preparation at room temperature with an analysis chamber pressure of 10^{-6} Pa.

The main peaks analyzed in the different samples were C *1s*, N *1s*, O *1s*, and Zn *2p*. Data treatment was executed with the CasaXPS software (Casa Software Ltd., Teignmouth, UK) using a Gaussian/ Lorentzian (85/15) decomposition treatment and a Shirley-type baseline subtraction. All XPS spectra were calibrated using the C-(C,H) component of the C *1s* peak localized at 284.8 eV.

3.3. Photocatalytic Experiments

In a quartz sealed round-bottom flask (Figure 12), 10 mg of each ZnO NPs were suspended in 10 mL of a PNP aqueous solution (1×10^{-4} mol.L^{-1}). The solutions were stirred and irradiated with two UV-A lamps (TL Mini Blacklight Blue, TL 8W BLB 1FM/10X25CC, λ_{max} = 370 nm, Philips, Amsterdam, The Nederlands). The best sample was also irradiated with four lamps. Aluminum foil was used to cover the outer wall of the reactor and prevent any side reactions with ambient light. A 2 mL sample was taken after 7 h of exposure to UV-A. ZnO catalysts were filtered off with a syringe filter (polypropylene, 13 mm diameter, 0.2 µm pore size, Whatman™, Maidstone, England). The concentration of PNP was measured by UV/Vis spectroscopy (1700 UV/visible spectrophotometer, Shimadzu) at 317 nm, which correspond to the acidic form of PNP. Previously, a calibration curve was made for the PNP acidic form. Previously, a control experiment was performed to assess if PNP does not undergo direct photolysis under this ultraviolet A (UVA) illumination.

It has been reported that if the degradation of PNP is not complete, specific peaks of the intermediate molecules appear in the range 200–500 nm of the UV/visible spectrum [34,35]. Due to the absence of these peaks during the measurements, complete mineralization can be considered here. Moreover, total mineralization of PNP during homologous photocatalytic tests using a similar installation has been shown in a previous work [36].

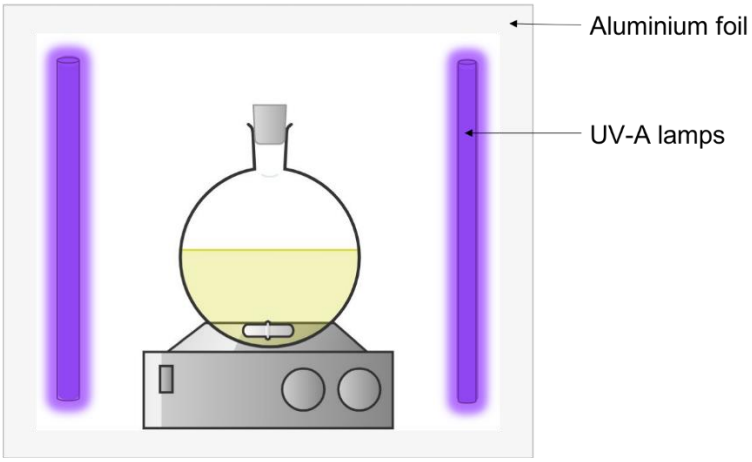

Figure 12. Schematic representation of the photocatalytic set used for the irradiation experiments.

3.4. Recycling Photocatalytic Experiments

To evaluate the stability of the photoactivity of ZnO materials, photocatalytic recycling experiments were carried out with the Z19 sample. The same protocol as explained in Section 3.3 was performed with this catalyst. After the first photocatalytic experiment, the sample was recovered by centrifugation (9000 rpm for 30 min) followed by drying at 120 °C overnight. A second and third cycle of photocatalytic tests as described above were applied to the re-used catalysts, with washing and drying steps between each photocata-

lytic experiment. So, the Z19 sample was used for three successive photocatalytic experiments, for a total of 21 h of illumination. A mean PNP degradation rate of the three experiments was calculated. An XRD measurement was performed after the three photocatalytic experiments in order to check the integrity of the crystalline material.

4. Conclusions

In this work, ZnO nanoparticles were synthesized by a sol-gel process, in order to obtain different morphologies in green conditions. The goals were to study both the influence of the synthesis parameters on the resulting morphology, and the influence of these different morphologies on the photocatalytic activity, for the degradation of an organic pollutant in water.

Two different experimental protocols were tested to produce ZnO. All the samples provided the same ZnO crystalline phase (wurtzite), according to PXRD patterns. In order to study the influence of the synthesis parameters on the resulting morphology, an experimental plan was designed with JMP® software, to study the influence of three parameters (pH, stirring (or not), and reaction time) in the first synthesis method, which was a sol-gel process performed at room temperature and using NaOH as a basic titrant. Many different sizes and morphologies were obtained, according to TEM images. A statistical study performed with JMP® software revealed that pH is the most influencing parameter in the crystallite size response for the ZnO prepared with this synthesis method.

The second synthesis process (sol-gel at 60 °C, using KOH as a basic titrant) provided ZnO nanoparticles with the most regular shape, the smallest size (8 nm from XRD), and with the highest dispersion.

In the second part of this work, the ZnO nanoparticles were tested in the degradation of a model water pollutant, namely, *p*-nitrophenol, by advanced oxidation processes, under UV-A light. The ZnO photocatalysts exhibited notable degradation after only 7 h. Nanoparticles with different shapes and sizes were tested. The obtained results indicated that the photoactivity of ZnO is mainly governed by the specific surface area. Optimization of the nanoparticle size was therefore also critical for the water decontamination application.

Moreover, comparison with a commercial TiO_2 photocatalyst (Evonik P25) showed that the best ZnO produced with this green process can reach similar photoactivity without a calcination step.

By normalization of the photodegradation by the specific surface area, the ZnO samples showed higher activities than the commercial photocatalyst, up to ten times. This suggests that if the specific surface area of the ZnO can be further increased, the photoactivity will reach a higher level than the commercial photocatalyst. It is important to be reminded that the ZnO materials were obtained with a green synthesis process, without an energy-consuming calcination step.

Supplementary Materials: The following are available online at www.mdpi.com/2073-4344/11/10/1182/s1, Figure S1: XRD diffraction patterns obtained for a ZnO sample (Z1) before and after washing; Figure S2: XPS spectra of Z19 ZnO sample: (a) Zn *2p* region, (b) O *1s* region, (c) N *1s* region and (d) C *1s* region; Figure S3: Observed d_{XRD} values in function of expected d_{XRD} by the built model. The red area and the blue line represent, respectively, the confidence interval and the mean value of the d_{XRD}; Figure S4: Effects summary. The blue line represents the LogWorth reference equal to two; Figure S5: evolution of the absorbance of PNP between 250 and 500 nm for pure PNP (blue line), after 7 h of UV-A irradiation: not filtered (red line), filtered (yellow line) and with a drop of HNO_3 (green line), in order to evaluate the effects of these parameters on the PNP absorbance before performing the photocatalytic experiments; Figure S6: XRD pattern of Z19 sample after three successive photocatalytic experiments in PNP degradation. Table S1: analysis of variance report.

Author Contributions: Conceptualization, methodology, J.G.M., L.L., and S.H.; investigation, analysis, J.G.M., L.L., T.H., N.B., S.D.K., R.H.M.M. and S.H.; writing—original draft preparation, J.G.M., L.L. and S.H.; supervision, funding acquisition and project administration, B.E., C.A.F. and S.H. All

the authors corrected the paper before submission and during the revision process. All authors have read and agreed to the published version of the manuscript.

Funding: This research was funded by Innoviris Brussels, through the Bridge project—COLORES.

Data Availability Statement: The raw/processed data required to reproduce these findings cannot be shared at this time as the data also forms part of an ongoing study.

Acknowledgments: S.H. and N.B. thank the Belgian National Funds for Scientific Research (F.R.S.-FNRS) for their Research Director position and Fund for Research Training in Industry and Agriculture (FRIA) grant, respectively. The authors thanks Jean-Francois Statsyns and François Devred for BET measurements and DRUVS measurements, respectively. The authors also thank Pr. Tom Leyssens for the JMP simulations.

Conflicts of Interest: The authors declare no conflict of interest.

References

1. Khan, M.A.; Ghouri, A.M. ENVIRONMENTAL POLLUTION: Its effects on life and its remedies. *J. Arts Sci. Commer.* **2011**, *2*, 276–285.
2. Qian, L.; Wang, S.; Xu, D.; Guo, Y.; Tang, X.; Wang, L. Treatment of municipal sewage sludge in supercritical water: A review. *Water Res.* **2016**, *89*, 118–131.
3. Macova, M.; Toze, S.; Hodgers, L.; Mueller, J.F.; Bartkow, M.; Escher, B.I. Bioanalytical tools for the evaluation of organic micropollutants during sewage treatment, water recycling and drinking water generation. *Water Res.* **2011**, *45*, 4238–4247.
4. Turolla, A.; Fumagalli, M.; Bestetti, M.; Antonelli, M. Electrophotocatalytic decolorization of an azo dye on TiO 2 self-organized nanotubes in a laboratory scale reactor. *Desalination* **2012**, *285*, 377–382.
5. Fox, K.R. Water Treatment and Equipment Decontamination Techniques. *J. Contemp. Water Res. Educ.* **2009**, *129*, 18–21.
6. Oturan, M.A.; Aaron, J.J. Advanced oxidation processes in water/wastewater treatment: Principles and applications. A review. *Crit. Rev. Environ. Sci. Technol.* **2014**, *44*, 2577–2641.
7. Verma, S.; Younis, S.A.; Kim, K.H.; Dong, F. Anisotropic ZnO nanostructures and their nanocomposites as an advanced platform for photocatalytic remediation. *J. Hazard. Mater.* **2021**, *415*, 125651.
8. Mahy, J.G.; Lambert, S.D.; Tilkin, R.G.; Poelman, D.; Wolfs, C.; Devred, F.; Gaigneaux, E.M.; Douven, S. Ambient temperature ZrO2-doped TiO2 crystalline photocatalysts : Highly efficient powders and films for water depollution. *Mater. Today Energy* **2019**, *13*, 312–322.
9. Alias, S.S.; Ismail, A.B.; Mohamad, A.A. Effect of pH on ZnO nanoparticle properties synthesized by sol-gel centrifugation. *J. Alloys Compd.* **2010**, *499*, 231–237.
10. Shamhari, N.M.; Wee, B.S.; Chin, S.F.; Kok, K.Y. Synthesis and characterization of zinc oxide nanoparticles with small particle size distribution. *Acta Chim. Slov.* **2018**, *65*, 578–585.
11. Khanizadeh, B.; Khosravi, M.; Behnajady, M.A.; Shamel, A.; Vahid, B. Mg and La Co-doped ZnO nanoparticles prepared by sol– gel method: Synthesis, characterization and photocatalytic activity. *Period. Polytech. Chem. Eng.* **2020**, *64*, 61–74.
12. Ong, C.B.; Ng, L.Y.; Mohammad, A.W. A review of ZnO nanoparticles as solar photocatalysts : Synthesis , mechanisms and applications. *Renew. Sustain. Energy Rev.* **2018**, *81*, 536–551.
13. Pirhashemi, M.; Habibi-Yangjeh, A.; Rahim Pouran, S. Review on the criteria anticipated for the fabrication of highly efficient ZnO-based visible-light-driven photocatalysts. *J. Ind. Eng. Chem.* **2018**, *62*, 1–25.
14. Talam, S.; Karumuri, S.R.; Gunnam, N. Synthesis, Characterization, and Spectroscopic Properties of ZnO Nanoparticles. *ISRN Nanotechnol.* **2012**, *2012*, 1–6.
15. Hasnidawani, J.N.; Azlina, H.N.; Norita, H.; Bonnia, N.N.; Ratim, S.; Ali, E.S. Synthesis of ZnO Nanostructures Using Sol-Gel Method. *Procedia Chem.* **2016**, *19*, 211–216.
16. Nagornov, I.A.; Mokrushin, A.S.; Simonenko, E.P.; Simonenko, N.P.; Gorobtsov, P.Y.; Sevastyanov, V.G.; Kuznetsov, N.T. Zinc oxide obtained by the solvothermal method with high sensitivity and selectivity to nitrogen dioxide. *Ceram. Int.* **2020**, *46*, 7756–7766.
17. Parashar, M.; Shukla, V.K.; Singh, R. Metal oxides nanoparticles via sol–gel method: A review on synthesis, characterization and applications. *J. Mater. Sci. Mater. Electron.* **2020**, *31*, 3729–3749.
18. Brinker, C.j.; Scherer, G.W. *Sol-Gel Science: The Physics and Chemistry of Sol-Gel Processing*; Academic Press: London, UK, 2013.
19. Léonard, G.L.M.; Pàez, C.A.; Ramírez, A.E.; Mahy, J.G.; Heinrichs, B. Interactions between Zn2+ or ZnO with TiO2 to produce an efficient photocatalytic, superhydrophilic and aesthetic glass. *J. Photochem. Photobiol. A Chem.* **2018**, *350*, 32–43.
20. Ba-Abbad, M.M.; Kadhum, A.A.H.; Bakar Mohamad, A.; Takriff, M.S.; Sopian, K. The effect of process parameters on the size of ZnO nanoparticles synthesized via the sol-gel technique. *J. Alloys Compd.* **2013**, *550*, 63–70.
21. Preethi, S.; Anitha, A.; Arulmozhi, M. A comparative analysis of the properties of zinc oxide (ZnO) nanoparticles synthesized by hydrothermal and sol-gel methods. *Indian J. Sci. Technol.* **2016**, *9*, 1–6.

22. Malengreaux, C.M.; Douven, S.; Poelman, D.; Heinrichs, B.; Bartlett, J.R. An ambient temperature aqueous sol–gel processing of efficient nanocrystalline doped TiO2-based photocatalysts for the degradation of organic pollutants. *J. Sol-Gel Sci. Technol.* **2014**, *71*, 557–570.
23. Mahy, J.G.; Cerfontaine, V.; Poelman, D.; Devred, F.; Gaigneaux, E.M.; Heinrichs, B.; Lambert, S.D. Highly efficient low-temperature N-doped TiO2 catalysts for visible light photocatalytic applications. *Materials* **2018**, *11*, 584.
24. Hargreaves, J.S.J. Some considerations related to the use of the Scherrer equation in powder X-ray diffraction as applied to heterogeneous catalysts. *Catal. Struct. React.* **2016**, *2*, 33–37.
25. Langfors, J.I.; Wilson, J.C. Seherrer after Sixty Years: A Survey and Some New Results in the Determination of Crystallite Size. *J. Appl. Crystallogr.* **1978**, *11*, 102–113.
26. Salvatore, D.; Reagle, D. *JMP Statistics and Graphics Guide*; SAS Institute Inc.: Cary, NC, USA, 2008; ISBN 0071395687.
27. Reza, M.; Khaki, D.; Saleh, M.; Aziz, A.; Raman, A.; Mohd, W.; Wan, A. Application of doped photocatalysts for organic pollutant degradation—A review. *J. Environ. Manag.* **2017**, *198*, 78–94.
28. Delsouz Khaki, M.R.; Shafeeyan, M.S.; Raman, A.A.A.; Daud, W.M.A.W. Evaluating the efficiency of nano-sized Cu doped TiO2/ZnO photocatalyst under visible light irradiation. *J. Mol. Liq.* **2018**, *258*, 354–365.
29. Mahy, J.G.; Lambert, S.D.; Léonard, G.L.M.; Zubiaur, A.; Olu, P.Y.; Mahmoud, A.; Boschini, F.; Heinrichs, B. Towards a large scale aqueous sol-gel synthesis of doped TiO2: Study of various metallic dopings for the photocatalytic degradation of p-nitrophenol. *J. Photochem. Photobiol. A Chem.* **2016**, *329*, 189–202.
30. López, R.; Gómez, R. Band-gap energy estimation from diffuse reflectance measurements on sol-gel and commercial TiO2: A comparative study. *J. Sol-Gel Sci. Technol.* **2012**, *61*, 1–7.
31. Benhebal, H.; Chaib, M.; Salmon, T.; Geens, J.; Leonard, A.; Lambert, S.D.; Crine, M.; Heinrichs, B. Photocatalytic degradation of phenol and benzoic acid using zinc oxide powders prepared by the sol-gel process. *Alexandria Eng. J.* **2013**, *52*, 517–523.
32. Fauduet, H. *Mécanique des Fluides et des Solides Appliquée à la Chimie*; Lavoisier: Paris, France, 2011; ISBN 274301315X.
33. Kubelka, P. New contributions to the optics of intensely light-scattering materials. *J. Opt. Soc. Am.* **1948**, *38*, 448–457.
34. Paola, A.D.; Augugliaro, V.; Palmisano, L.; Pantaleo, G.; Savinov, E. Heterogeneous photocatalytic degradation of nitrophenols. *J. Photochem. Photobiol. A: Chem.* **2003**, *155*, 207–214.
35. Augugliaro, V.; Palmisano, L.; Schiavello, M.; Sclafani, A.; Marchese, L.; Martra, G.; Miano, F. Photocatalytic degradation of nitrophenols in aqueous titanium dioxide dispersion. *Appl. Catal.* **1991**, *69*, 323–340.
36. Malengreaux, C.M.; Léonard, G.M.-L.; Pirard, S.L.; Cimieri, I.; Lambert, S.D.; Bartlett, J.R.; Heinrichs, B. How to modify the photocatalytic activity of TiO2 thin films through their roughness by using additives. A relation between kinetics, morphology and synthesis. *Chem. Eng. J.* **2014**, *243*, 537–548.